RESEARCH ARTICLE | AUGUST 26 2024

Evaluating impedance boundary conditions to model interfacial dynamics in acoustofluidics *⊙*

Khemraj Gautam Kshetri 📵 ; Nitesh Nama 🗷 📵



Physics of Fluids 36, 082009 (2024)

https://doi.org/10.1063/5.0225930

A CHORUS





Articles You May Be Interested In

Quantitative assessment of parallel acoustofluidic device

J. Acoust. Soc. Am. (July 2021)

Introduction to the special issue on the theory and applications of acoustofluidics

J Acoust Soc Am (December 2021)

Full-wave modeling of micro-acoustofluidic devices driven by standing surface acoustic waves for microparticle acoustophoresis

J. Appl. Phys. (September 2020)



Physics of Fluids

Special Topics Open for Submissions

Learn More



Evaluating impedance boundary conditions to model interfacial dynamics in acoustofluidics

Cite as: Phys. Fluids **36**, 082009 (2024); doi: 10.1063/5.0225930

Submitted: 27 June 2024 · Accepted: 6 August 2024 ·

Published Online: 26 August 2024







Khemraj Gautam Kshetri (ib) and Nitesh Nama (ib)



AFFILIATIONS

Department of Mechanical & Materials Engineering, University of Nebraska-Lincoln, Lincoln, Nebraska 68588, USA

^{a)}Also at: Nebraska Center for Integrated Biomolecular Communication, University of Nebraska-Lincoln, Lincoln, NE 68588, USA. Author to whom correspondence should be addressed: nitesh.nama@unl.edu

ABSTRACT

We present a numerical study to investigate the efficacy of impedance boundary conditions in capturing the interfacial dynamics of a particle subjected to an acoustic field and study the concomitant time-averaged acoustic streaming and radiation force fields. While impedance boundary conditions have been utilized to represent fluid-solid interface in acoustofluidics, such models assume the solid material to be locally reactive to the acoustic waves. However, there is a limited understanding of when this assumption holds true, raising concerns about the suitability of impedance boundary conditions. Here, we systematically investigate the applicability of impedance boundary conditions by comparing the predictions of an impedance boundary approach against a fully coupled fluid-solid model. We contrast the oscillation profiles of the fluid-solid interface predicted by the two models. We consider different scatterer materials to identify the extent to which the differences in interfacial dynamics impact the time-averaged fields and highlight the divergence within the predictions of the two models. Our findings indicate that, although impedance boundary conditions can yield qualitatively similar results to the full model in certain situations, the predictions from the two models generally differ both qualitatively and quantitatively. These results underscore the importance of exercising caution when applying these boundary conditions to model general acoustofluidic systems.

Published under an exclusive license by AIP Publishing. https://doi.org/10.1063/5.0225930

I. INTRODUCTION

Acoustofluidic systems have rapidly emerged as a promising frontier of lab-on-a-chip technologies, in part due to their exciting potential for manipulating fluids and particles at microscales.^{1,2} These systems allow contact-free handling of fluids and particles and have been utilized for several applications including fluid mixing and pumping,^{3,4} particle trapping,^{5,6} microswimming,⁷ and more recently, for integration with robotics to demonstrate rapid and automatic execution of common laboratory functionalities.8 Acoustofluidic devices frequently leverage scattering of acoustic waves from solid surfaces (such as the walls of microfluidic channels or the scatterers immersed within a fluid domain) to generate acoustic streaming and radiation force fields. For modeling such systems, the fluid-solid interface is usually represented in one of the following two ways. The first approach solves a coupled fluid-solid problem by prescribing velocity and traction continuity boundary conditions at the interface. In contrast, the second approach solves a fluid-only system and employs boundary conditions at the fluid domain boundaries to account for the presence of solid walls. For instance, in the limit of "acoustically hard" material, the fluid-solid interface can be modeled via a "hard-wall boundary

condition" that prescribes a homogeneous Dirichlet boundary condition on the acoustic velocity. This boundary condition has been widely used in modeling of bulk acoustic wave devices to model siliconewater and glass-water interface. 9,10 Similarly, in the opposite limit (i.e., for "acoustically-soft" material), the fluid-solid interface is typically prescribed a traction-free boundary condition to model the liquid-air interface in droplet acoustofluidics. 9,11 For general polymer materials that lie between these two limits, typically an impedance boundary condition has been employed to represent the interface. 12-23 This approach accounts for the difference in the acoustic impedance of the fluid and solid material by prescribing a Robin (or mixed) boundary condition that relates the acoustic velocity and pressure at the boundary.

While several models using impedance boundary conditions have yielded predictions similar to the experimental results, the use of these boundary conditions relies on the assumption that the fluid-solid interface is locally reactive to the acoustic waves. 16-18,20-22 However, the applicability of this assumption for common scatterer materials subjected to high frequencies employed in micro-acoustofluidics is unclear, leading to questions concerning their applicability.¹⁴

Furthermore, the impact of the use of impedance boundary conditions on the time-averaged acoustic streaming and radiation force fields remains unknown.

In this work, we investigate the applicability of impedance boundary conditions by comparing the predictions of an impedance boundary approach against a fully coupled fluid-solid model. To this end, we consider a solid particle subjected to a standing acoustic wave and contrast the fluid-solid interfacial dynamics and the resulting time-averaged fields predicted by the two models. We consider different scatterer materials to investigate the impact of these differences in interfacial dynamics on the time-averaged fields and highlight the divergence within the predictions of the two models. Our results suggest that the impedance boundary conditions—despite producing qualitatively similar results to experiments for certain scenarios—are not generally appropriate to study time-averaged acoustic fields and highlight the need for prudence in employing these boundary conditions to model acoustofluidic systems.

II. THEORY

A. Governing equations for fluid

The system of equations governing the motion of a linear viscous compressible fluid is given by the balance laws for mass and linear momentum and the equation of state as

$$\frac{\partial \rho}{\partial t} + \nabla \cdot (\rho \mathbf{v}) = 0, \tag{1}$$

$$\rho \frac{\partial \boldsymbol{v}}{\partial t} + \rho(\nabla \boldsymbol{v}) \boldsymbol{v} = \nabla \cdot \boldsymbol{\sigma}, \tag{2}$$

$$p = p(\rho), \tag{3}$$

with

$$\boldsymbol{\sigma} = -p\mathbf{I} + \eta(\nabla \boldsymbol{v} + (\nabla \boldsymbol{v})^{\mathrm{T}}) + \left(\eta_{\mathrm{b}} - \frac{2\eta}{3}\right)(\nabla \cdot \boldsymbol{v})\mathbf{I}, \tag{4}$$

$$\frac{\partial \rho_1}{\partial t} + \rho_0(\nabla \cdot \boldsymbol{v}_1) = 0, \tag{5}$$

$$\rho_0 \frac{\partial \boldsymbol{v}_1}{\partial t} = \nabla \cdot \boldsymbol{\sigma}_1, \tag{6}$$

$$p_1 = c_0^2 \rho_1, (7)$$

with

$$\boldsymbol{\sigma}_{1} = -p_{1}\mathbf{I} + \eta(\nabla \boldsymbol{v}_{1} + (\nabla \boldsymbol{v}_{1})^{\mathrm{T}}) + \left(\eta_{b} - \frac{2\eta}{3}\right)(\nabla \cdot \boldsymbol{v}_{1})\mathbf{I}, \quad (8)$$

where c_0 is the speed of sound in the fluid. To numerically calculate the response of a fluid–solid system under a prescribed acoustic field,

we segregate the total first-order fields into their incident (or background) and scattered components: $\phi = \phi^{bg} + \phi^{sc}$. Here, the background field denotes the prescribed acoustic field and the scattered field is computed by solving the first-order system of equations.²⁷ In this work, we take the background field to be a one-dimensional plane standing wave along the *y*-direction,

$$v_1^{\text{bg}} = \frac{\psi_a}{2} i k \left(e^{i(ky+\varphi)} - e^{-i(ky+\varphi)} \right) e^{i\omega t} \boldsymbol{e}_y, \tag{9}$$

where ω is the angular frequency, $k=\frac{\omega}{c_0}-\alpha i$ is the wave number with $\alpha=\frac{\omega^2\eta}{2c_0^2\rho_0}\left(\frac{\eta_b}{\eta}+\frac{4}{3}\right)$ being the attenuation coefficient, φ is the phase shift, \boldsymbol{e}_y is the unit vector along the y-direction, and ψ_a is the velocity potential amplitude,

$$\psi_{\rm a} = -\frac{p_{\rm a}}{i\omega\rho_{\rm 0} + \left(\eta_{\rm b} + \frac{4}{3}\eta\right)k^2},\tag{10}$$

with $p_{\rm a}$ being the pressure amplitude. Noting that the first-order terms in the perturbation approach are representative of the system's harmonic response to the acoustic actuation, they are taken to be harmonic in time (with an $e^{i\omega t}$ dependence in time).

To derive the governing equations for the fluid's steady response at the second-order, we substitute the perturbation expansion of primary variables into the governing equations and time average the resulting equations to obtain

$$\rho_0 \nabla \cdot \langle \boldsymbol{v}_2 \rangle = -\nabla \cdot \langle \rho_1 \boldsymbol{v}_1 \rangle, \tag{11}$$

$$\left\langle \rho_1 \frac{\partial v_1}{\partial t} \right\rangle + \rho_0 \langle (\nabla v_1) v_1 \rangle = \nabla \cdot \boldsymbol{\sigma}_2,$$
 (12)

with

$$\sigma_{2} = -\langle p_{2}\rangle \mathbf{I} + \eta(\nabla\langle \boldsymbol{v}_{2}\rangle + (\nabla\langle \boldsymbol{v}_{2}\rangle)^{T}) + \left(\eta_{b} - \frac{2\eta}{3}\right)(\nabla \cdot \langle \boldsymbol{v}_{2}\rangle)\mathbf{I},$$
(13)

where $\langle A \rangle$ represents the time average of A over the oscillation time period T, $\langle A \rangle := \frac{1}{T} \int_T A dt$.

B. Governing equations for solid

In the absence of body forces, the balance of linear momentum for a solid can be expressed as

$$\rho_{\rm s} \frac{\partial^2 \mathbf{u}}{\partial t^2} = \nabla \cdot \mathbf{\sigma}_{\rm s},\tag{14}$$

where ρ_s and \boldsymbol{u} are the solid's density and displacement vector, respectively, and $\boldsymbol{\sigma}_s$ denotes the solid's stress tensor. The solid scatterer and the channel walls are taken to be linear elastic such that the stress tensor can be expressed as

$$\sigma_{s} = \lambda_{s}(\operatorname{tr} \boldsymbol{\varepsilon})\mathbf{I} + 2\mu_{s}\boldsymbol{\varepsilon}, \quad \boldsymbol{\varepsilon} = \frac{1}{2}\left[\nabla \boldsymbol{u} + (\nabla \boldsymbol{u})^{T}\right],$$
 (15)

where λ_s and μ_s are Lamé parameters. Given the purely elastic nature of the solid, its response to acoustic actuation is purely harmonic (i.e., there are no second-order contributions within the solid domain).

Thus, the total displacement of the solid, u, is harmonic in time and is coupled to the fluid's first order velocity v_1 at the fluid-solid interface.

C. Acoustic radiation force

In addition to the second-order streaming flow, another time-averaged quantity of interest in acoustofluidic systems is the acoustic radiation force experienced by immersed microparticles. Following Settnes and Bruus, ²⁹ the acoustic radiation force experienced by a spherical particle of radius a that is much smaller than the acoustic wavelength λ , mass density $\rho_{\rm p}$, and compressibility $\kappa_{\rm p}$ can be expressed as

$$\mathbf{F}^{\text{rad}} = -\pi a^3 \left[\frac{2\kappa_0}{3} \operatorname{Re} \left[f_0^* p_1^* \nabla p_1 \right] - \rho_0 \operatorname{Re} \left[f_1^* \mathbf{v}_1^* \cdot \nabla \mathbf{v}_1 \right] \right], \tag{16}$$

where $\kappa_0 = 1/(\rho_0 c_0^2)$ is the compressibility of the fluid, A^* denotes the complex conjugate of the quantity A, and the factors f_0 and f_1 are given as²⁹

$$f_0 = 1 - \frac{\kappa_p}{\kappa_0}, \quad f_1 = \frac{2(1 - \gamma)(\rho_p - \rho_0)}{2\rho_p + \rho_0(1 - 3\gamma)},$$
 (17)

with

$$\gamma = -\frac{3}{2} \left[1 + i(1 + \tilde{\delta}) \right] \tilde{\delta}, \quad \tilde{\delta} = \frac{\delta}{a}, \quad \delta = \sqrt{\frac{2\eta}{\omega \rho_0}}, \quad (18)$$

where δ denotes the thickness of the viscous boundary layer. We remark that Eq. (16) does not account for the microstreaming contributions to the acoustic radiation force. However, these contributions have been shown to be insignificant for the physical regime considered in this study where the thickness of the viscous boundary layer is smaller than the radius of the immersed microparticle, $\delta/a < 1$.

D. Numerical models and boundary conditions

Our model system comprises a cylindrical scatterer with radius $a_{\rm scat} = 5 \, \mu \rm m$ that is immersed within a surrounding fluid [Fig. 1(a)]. The entire system is subjected to a background standing acoustic wave along the y direction. The fluid domain is surrounded by a perfectly matched layer to absorb all the outgoing waves. Additionally, the fluid domain thickness is chosen to be sufficiently large to avoid the impact of outer boundaries on the streaming field around the scatterer. In our analysis, a fluid domain thickness of 200 $a_{\rm scat}$ was found to be adequate, which agrees well with prior reports. Referring to Figs. 1(a) and 1(b), we consider two different models that differ in their representation of the (first-order) acoustic boundary condition at the fluid–solid interface. Next, we describe the details of the two models and their associated boundary conditions.

1. Fluid-solid interaction model

The first model [Fig. 1(a)] considers a coupled fluid-solid problem by solving the governing equations for both the fluid and the solid and prescribes the continuity of velocity and traction at the fluid-solid interface as

$$v_1 = v_s, \quad \sigma_1 n_f = \sigma_s n_s, \quad \text{on} \quad \Gamma^{f,s},$$
 (19)

where $v_s = i\omega u$ represents the solid's velocity, and n_f and n_s are the unit normal vector to the fluid-solid interface pointing outward from

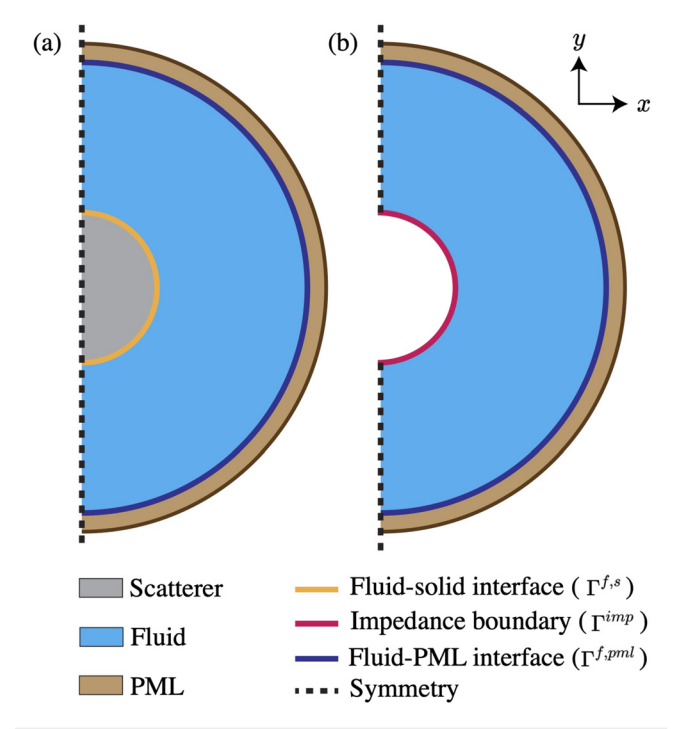


FIG. 1. Schematic of the model system and the associated boundary conditions. (a) Computational domain considered in the fluid–solid model comprising of a scatterer placed in the fluid. (b) Computational domain considered in the impedance model where the scatterer is replaced by the impedance boundary condition. In both cases, the fluid is surrounded by a perfectly matched layer (PML) to absorb outgoing waves, and the system is subjected to a standing wave in the *y* direction. Note that the figure is not drawn to scale.

the fluid and the solid domain, respectively. Since there are no secondorder contributions in the solid domain, the second-order problem is solved only in the fluid domain by prescribing a Dirichlet boundary condition on the second-order velocity as

$$\langle \boldsymbol{v}_2 \rangle = - \left\langle (\nabla \boldsymbol{v}_1) \frac{\boldsymbol{v}_1}{i\omega} \right\rangle, \quad \text{on} \quad \Gamma^{f,s} \cup \Gamma^{f,pml},$$
 (20)

where the term on the right-hand side represents the negative of the Stokes' drift at the interface. 3,27,31

2. Impedance model

The impedance model [Fig. 1(b)] estimates the reflections and transmissions at the fluid–solid interface by approximating the wave dynamics in the solid medium. Here, we outline the derivation of the commonly employed impedance boundary condition in the acousto-fluidics literature. To this end, consider a planar configuration with the liquid placed in the half space x < 0 in conjunction with a medium in x > 0. The wave dynamics in the medium is assumed to be governed by Eqs. (6) and (8) without the viscous terms, and the radiative loss in the medium is described by a right-ward propagating wave with potential $\phi_m = Ae^{-ik_m x}$. Accordingly, the x component of the velocity in the medium is obtained as $v_{mx} = \nabla \phi_m \cdot \mathbf{e}_x = -ik_m \phi_m$, with \mathbf{e}_x being the unit vector along the x axis. Similarly, the pressure can be expressed in terms of the potential as $p_m = -i\omega \rho_m \phi_m$ with ρ_m

being the medium density. Consequently, the pressure and the velocity in the medium can be related as $p_m = \rho_m c_m v_{nx} = \rho_m c_m v_{1x}$, where the continuity of velocity at the interface is utilized to equate the x component of velocity in liquid to that in the medium, $v_{1x} = v_{mx}$. For a curved surface with outward unit normal n_m , this relation is generalized as $p_m = \rho_m c_m v_1 \cdot n_f$, and the traction at the interface is given as $\sigma_m n_m = -p_m n_m = \rho_m c_m (v_1 \cdot n_f) n_f$. Substituting this expression in the right-hand side of the second relation in Eq. (19), the fluid traction at the interface is obtained as $\sigma_1 n_f = Z_s(v_1 \cdot n_f) n_f$, where $Z_s = \rho_s c_s$ denotes the acoustic impedance of the solid scatterer with c_s being the longitudinal speed of sound in the scatterer material. Finally, considering the normal component of this traction, we obtain the impedance boundary condition relating the normal traction and velocity at a point on the interface as

$$(\boldsymbol{\sigma}_1 \boldsymbol{n}_f) \cdot \boldsymbol{n}_f = Z_s(\boldsymbol{v}_1 \cdot \boldsymbol{n}_f) \quad \text{on} \quad \Gamma^{imp}.$$
 (21)

Furthermore, it is assumed that there is no significant wave motion in the tangential direction such that the tangential velocity at the interface is constrained to be zero. In essence, the impedance boundary condition is an approximation of the traction applied by the medium on the liquid and circumvents the need to solve for the solid's acoustic response by prescribing a relation between the local traction and the local normal velocity at the interface. In other words, the impedance boundary approach considers the solid material to be locally reactive to the acoustic waves such that the motion at any point on the interface can be considered to be dependent only on the traction at this point regardless of the traction distribution over the remaining surface. 21,22 Finally, we remark that this difference in first-order interfacial boundary condition is the primary difference between the impedance model and the coupled fluid-solid model and the second-order problem is treated similarly in two models by prescribing a Dirichlet boundary condition on the second-order velocity given by Eq. (20).

III. RESULTS

A. Acoustic fields

We first consider a glass scatterer (diameter = $10 \, \mu m$) immersed within a fluid (water) domain, which is subjected to a background standing wave field along the y direction. This material choice is motivated from the recent glass-capillary-based micro-robotic system reported by Durrer et al.⁸ The scatterer is placed at the velocity antinode of the background standing wave field ($\varphi = \pi/2$) and the acoustic frequency is taken to be 900 kHz. The relevant material properties are listed in Tables I and II. The acoustic pressure amplitude (p_a) is

TABLE I. The material parameters for the scatterer material considered in this work. The viscous acoustic contrast factors $(\Phi_{\text{visc}} = \frac{1}{3} \operatorname{Re}[f_0] + \frac{1}{2} \operatorname{Re}[f_1])$ are calculated considering water as surrounding fluid at an acoustic frequency of 900 kHz.

	$\begin{array}{c} \rho_{\rm p} \\ ({\rm kgm^{-3}}) \end{array}$	$(m s^{-1})$	$(m s^{-1})$	$\Phi_{ m visc}$
PDMS	1030	1030	110	-0.33
PMMA	1180	2757	1400	0.26
Glass	2240	5100	2800	0.56
Cu	8930	5010	2270	0.81
Au	19700	3240	1280	0.87

TABLE II. The material properties of the fluid (water). The viscous boundary layer thickness is calculated using Eq. (18) for an acoustic frequency of 900 kHz.

$\frac{\rho_0}{(\text{kg m}^{-3})}$	η (mPa s)	η _b (mPa s)	$\frac{c_0}{({\rm m}{\rm s}^{-1})}$	δ (μm)
998.2	1.002	3.09	1482	3.99

taken to be 500 kPa throughout this work. To understand the acoustic response of this system and the associated fluid–solid interfacial dynamics, we begin by computing the first-order velocity and pressure fields from both the fluid–solid and impedance models.

Figures 2(a) and 2(b) plot the amplitude of the x and y component of the scattered velocity field $(v_1^{\rm sc})$, respectively, while Fig. 2(c) plots the amplitude of the scattered pressure field $(p_1^{\rm sc})$ obtained from the fluid–solid model. Figures 2(d)–2(f) plot the corresponding results obtained from the impedance model. The two models exhibit excellent qualitative agreement, but significant quantitative differences exist. Comparing the range of numerical solutions in Figs. 2(a)–2(c) and Figs. 2(d)–2(f), the impedance model results in significantly stronger scattered acoustic fields and overpredicts both the scattered velocity and pressure solutions. Specifically, the maximum value for each panel in the impedance solutions is approximately 2.8 times of the predictions from the fluid–solid model. To investigate the origins of these differences, we inspect the time-varying oscillation profile of the fluid–solid interface predicted from the two models. Figure 3 shows arrow plots of the total velocity field at the interface from the two models at

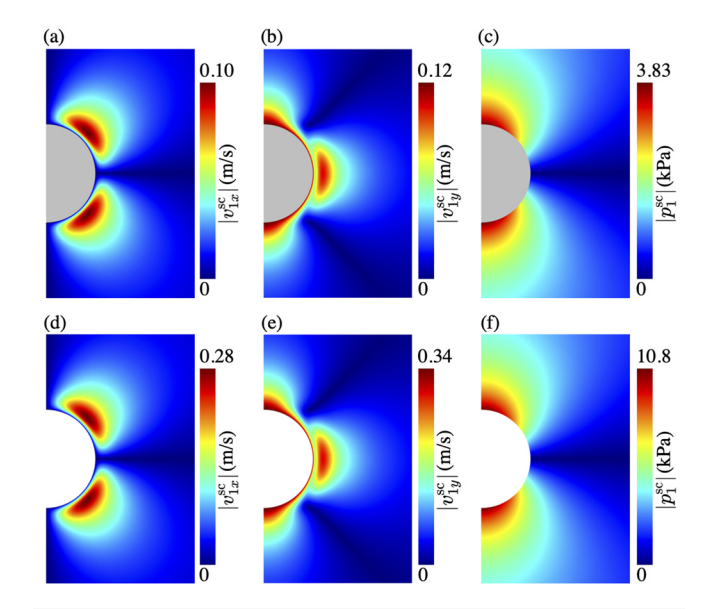


FIG. 2. Scattered acoustic fields around a 10 μm diameter glass scatterer immersed in water and subjected to an acoustic wave of 900 kHz. Numerical predictions of the fluid–solid model for the amplitude of the (a) x and (b) y components of the scattered velocity field, and (c) the scattered pressure field. (d)–(f) Corresponding predictions from the impedance model. While the two models yield qualitatively similar results, the impedance model significantly overpredicts all the fields. The different scales on the color bar are chosen to highlight qualitative similarity between the predictions of the two models.

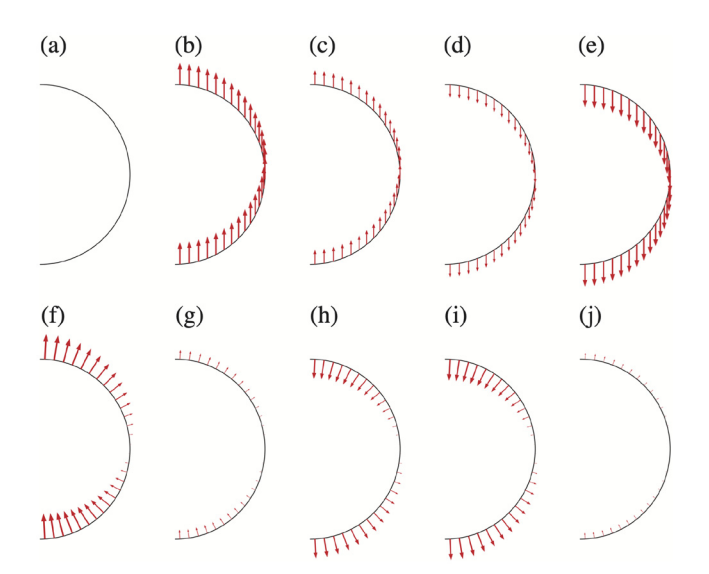


FIG. 3. (a)–(e) Velocity vectors at the solid–fluid interface at t=0, T/5, 2T/5, 3T/5, and 4T/5, respectively, obtained from the fluid–solid model, where T denotes the acoustic time period. (f)–(j) Corresponding results from the impedance model. Note that the arrow lengths are normalized against the respective amplitudes of the total velocity field from the fluid–solid and the impedance model.

different time instances within an oscillation period. The two models yield entirely different oscillatory dynamics of the fluid–solid interface. Specifically, the total velocity at the interface in the fluid–solid model is approximately parallel to the *y* direction at all times, suggesting a largely translational oscillation mode. In contrast, the total velocity at the interface from the impedance model is aligned along the normal to the interface, suggesting shape oscillations of the interface. This observation is consistent with the fact that the impedance model prescribes a zero tangential velocity at the interface; therefore, the interface oscillates completely along the normal direction.

To further examine the oscillatory dynamics of the interface, Fig. 4 plots the background, scattered, and total velocity as a function of time at a representative point located in the upper half of the interface at 45° with respect to the x axis. Panels (a) and (b) plot the x and y components, respectively, of these velocity fields obtained from the fluid–solid model, while panels (c) and (d) plot the corresponding results from the impedance model. Referring to Figs. 4(a) and 4(c), the x components of the scattered and total field are equal to each other for both models since the prescribed background field is a standing wave field along the y direction, and its x component is zero. The scattering is observed to be significantly stronger in the impedance model with the amplitude of the scattered field being three orders of magnitude larger than that in the fluid–solid model.

Next, we turn our attention to the results for the y component from fluid–solid model, plotted in Fig. 4(b). It can be observed that the background, scattered, and total fields are of the same order of magnitude. Note that the y component of the total field is five orders of magnitude larger than its x component [panel (a)], resulting in a total field that is almost parallel to the y axis, as seen in Figs. 3(a)–3(e). Comparing Fig. 4(c) with the y component predicted by the impedance model in Fig. 4(d), we observe significant differences. Specifically, the scattering is observed to be much stronger in the impedance model

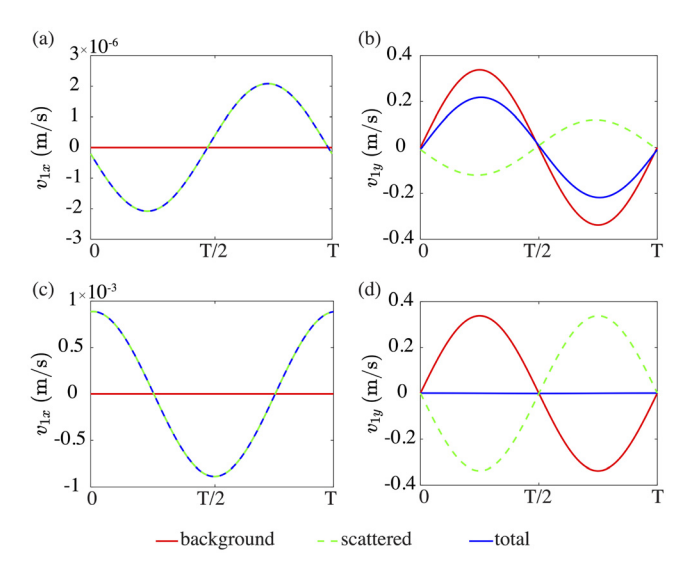


FIG. 4. Plots of the background, scattered, and total velocity field as a function of time for a representative point located in the upper half of the interface at 45° with respect to the x axis. (a) x and (b) y components of velocity fields obtained from the fluid–solid model. (c) and (d) Corresponding predictions from the impedance model.

such that the scattered velocity almost completely cancels out the background velocity and yields a total velocity amplitude that is over two orders of magnitude smaller than the background and the scattered velocities. Indeed, the y component of the total field is of the same order of magnitude as the x component, resulting in a total velocity field pointed along the normal direction as shown in Figs. 3(f)-3(j). These results illustrate that the impedance model significantly overpredicts the scattering velocity, which almost completely cancels out the prescribed background velocity and yields a total velocity field that is several orders of magnitude smaller than that predicted by the fluid-solid model. From a physical perspective, this suggests that the impedance model fails to completely capture the compliant nature of the fluid-solid interface and predicts scattering results that are representative of a significantly more rigid material.

B. Time-averaged fields

Given that both the radiation force and the streaming velocity depend on the first-order fields and their gradients, the differences in first-order fields can be expected to lead to varying predictions of the time-averaged fields. Noting this, we investigate the impact of differences in oscillatory dynamics of fluid-solid interface on the timeaveraged fields by comparing the predicted acoustic streaming and radiation force fields from the two models. The radiation force field is obtained by considering a 1 μ m polystyrene bead in Eq. (16). Figures 5(a) and 5(b) plot the radiation force and streaming field obtained from the fluid-solid model corresponding to the interfacial dynamics in Figs. 4(a) and 4(b), while Figs. 5(c) and 5(d) plot the results from the impedance model corresponding to the interfacial dynamics in Figs. 4(c) and 4(d). Comparing the radiation force fields in Figs. 5(a) and 5(c), it can be observed that the variations in the underlying interfacial dynamics in the two models lead to significant qualitative differences in the radiation force field close to the fluid-solid interface. The

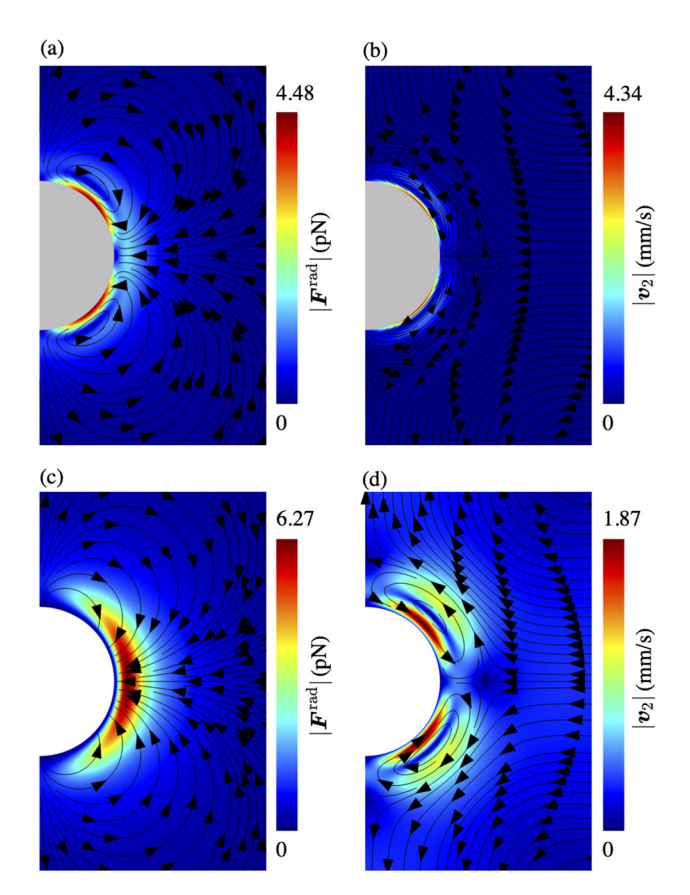


FIG. 5. Time-averaged fields around a 10 μ m diameter glass scatterer immersed in water and subjected to an acoustic wave of 900 kHz. (a) Radiation force and (b) streaming field obtained from the fluid–solid model corresponding to the interfacial dynamics in Figs. 4(a) and 4(b). (c) Radiation force field and (d) streaming field obtained from the impedance model corresponding to the interfacial dynamics in Figs. 4(c) and 4(d).

solution from the fluid-solid model is characterized by the presence of a pair of vortices that is absent in the impedance solution. Furthermore, similar to the first-order quantities, the impedance model overpredicts the maximum radiation force by approximately 40% (6.27 pN for the impedance model vs 4.48 pN for the fluid-solid model). Additionally, the location of maximum radiation force differs between the two solutions.

Next, we assess the impact of the varying interfacial dynamics in the two models on the streaming velocity [Figs. 5(b) and 5(d)]. In contrast to the radiation force results, the impedance model underpredicts the maximum streaming field by approximately 56% (1.87 mm/s for the impedance model vs 4.34 m/s for the fluid–solid model), which is consistent with the underprediction of the total acoustic velocity (see Fig. 4). In addition, the location of maximum velocity field is observed to be closer to the interface in the fluid–solid model. Interestingly, the solution from the fluid–solid model is characterized by two pairs of vortices in the vicinity of the scatterer but the innermost pair of vortices is absent in the impedance solution.

To further investigate the absence of the innermost vortices in impedance solution, Figs. 6(a) and 6(c) plot the second-order velocity

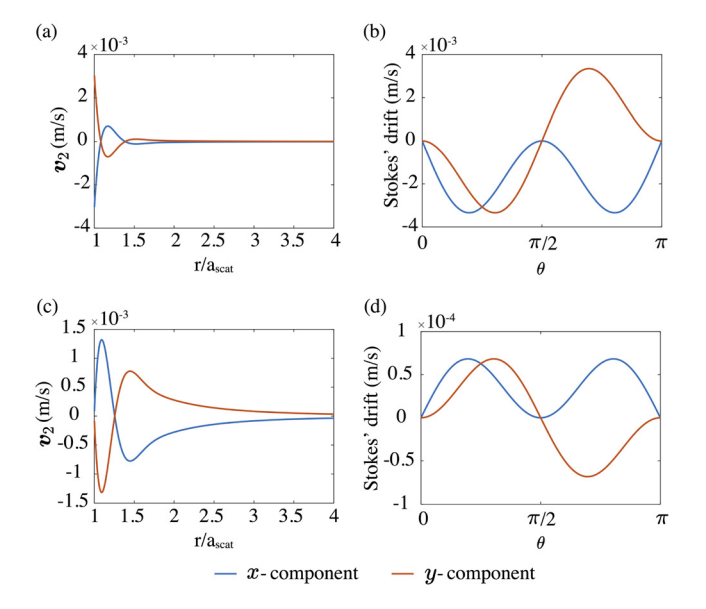


FIG. 6. (a) Streaming velocity along a radial line drawn at 45° from the x axis and (b) individual components of Stokes' drift along the fluid–solid interface obtained with the interfacial dynamics from the fluid–solid model. (c) and (d) Corresponding results obtained with the interfacial dynamics from the impedance model.

components obtained from the two models along a radial line drawn at 45° from the x axis. In line with the observation of the two pair of vortices in the fluid-solid model, the streaming velocity components intersect the x axis two times (e.g., v_2^x starts from a negative value at the interface, becomes zero at the center of the first vortex, and then again becomes zero at the center of the second vortex). In contrast, the streaming velocity components in the impedance solution intersect the x axis only once (e.g., v_2^x starts from a positive value at the interface and becomes zero at the center of the first vortex). Furthermore, the two models predict opposite direction of the streaming velocity at the interface. Noting that the streaming velocity at the interface is prescribed to be equal to the negative of the Stokes' drift [see Eq. (20)] in both models, the opposing streaming velocity directions at the interface imply that the two models must yield opposing directions of the Stokes' drift at the interface. This is confirmed by Figs. 6(b) and 6(d), which plot Stokes' drift along the fluid-solid interface. Both the individual components and the overall Stokes' drift differ in their sign between the two models, which results in opposite streaming velocity at the interface. Furthermore, the impedance solution underpredicts Stokes' drift by almost two orders of magnitude. Given that the Stokes' drift is an input to the second-order problem (via the velocity boundary condition at the interface), this may explain the lower values of maximum streaming velocity in impedance solution [Fig. 5(d)] compared to the fluidsolid model [Fig. 5(b)].

Overall, the results in Secs. III A and III B indicate that the impedance model may predict qualitatively similar results for the (first-order) acoustic fields, but significant quantitative differences exist between the predictions of the two models. These differences, in turn, yield time-averaged fields that differ both qualitatively and quantitatively between the two models.

C. Impact of scatterer material

Having investigated the acoustic and time-averaged fields for a specific choice of scatterer material, we now explore the time-averaged fields predicted by the two models for different choices of scatterer material. This analysis allows us to assess the impact of fluid-solid interfacial dynamics on streaming and radiation force fields in relation to different material choices and assess the efficacy of the impedance model for predicting time-averaged fields. We consider a similar configuration as in Secs. III A and III B, but with four different choices for the scatterer material: polydimethylsiloxane (PDMS), polymethyl methacrylate (PMMA), copper, and gold. Considering the surrounding fluid to be water and using the material properties listed in Tables I and II, their respective viscous acoustic contrast factor at 900 kHz are -0.33, 0.26, 0.81, and 0.87. The first two materials are commonly used in microfluidics settings, while copper and gold can be viewed as being closer to the limiting case of a rigid material (with compressibility approaching zero, and density much larger than that of the surrounding fluid).

Figure 7 compares the radiation force field obtained from the fluid-solid [panels (a)–(d)] and the impedance model [panels (e)–(h)] for the four scatterer materials. It can be observed that for both the models, the maximum value of the acoustic radiation force increases with increasing acoustic contrast factor. Nonetheless, the degree of

agreement between the two models varies significantly with material choice. First, comparing the results for the materials with relatively low acoustic contrast factors (PDMS and PMMA), the fluid-solid model [panels (a) and (b)] predicts a pair of vortices near the interface, which is absent in the impedance solution [panels (e) and (f)]. The impedance solution overpredicts the maximum radiation force by a factor of 23 for PDMS (0.26 pN for fluid-solid model vs 6.22 pN for impedance model) and 4.6 for PMMA (1.35 pN for fluid-solid model vs 6.26 pN for impedance model). Furthermore, the fluid-solid solution exhibits two symmetrically located maxima of acoustic radiation force, while the impedance solution is characterized by a single maxima located along the x axis. In contrast, for materials with relatively higher acoustic contrast factor (copper and gold), both the models exhibit one maxima of radiation force, located along the x axis. Nonetheless, the fluid-solid solution is still characterized by a pair of vortices that are absent in the impedance solution. While the impedance solution continues to overpredict the maximum radiation force, the factor of overprediction (1.4 for copper and 1.17 for gold) decreases with increase in the acoustic contrast factor.

It is also interesting to note that while the fluid-solid model exhibits both qualitative and quantitative variation among different materials, the impedance solution is rather insensitive to the material choice. Specifically, referring to panels (a)–(d), as the acoustic contrast

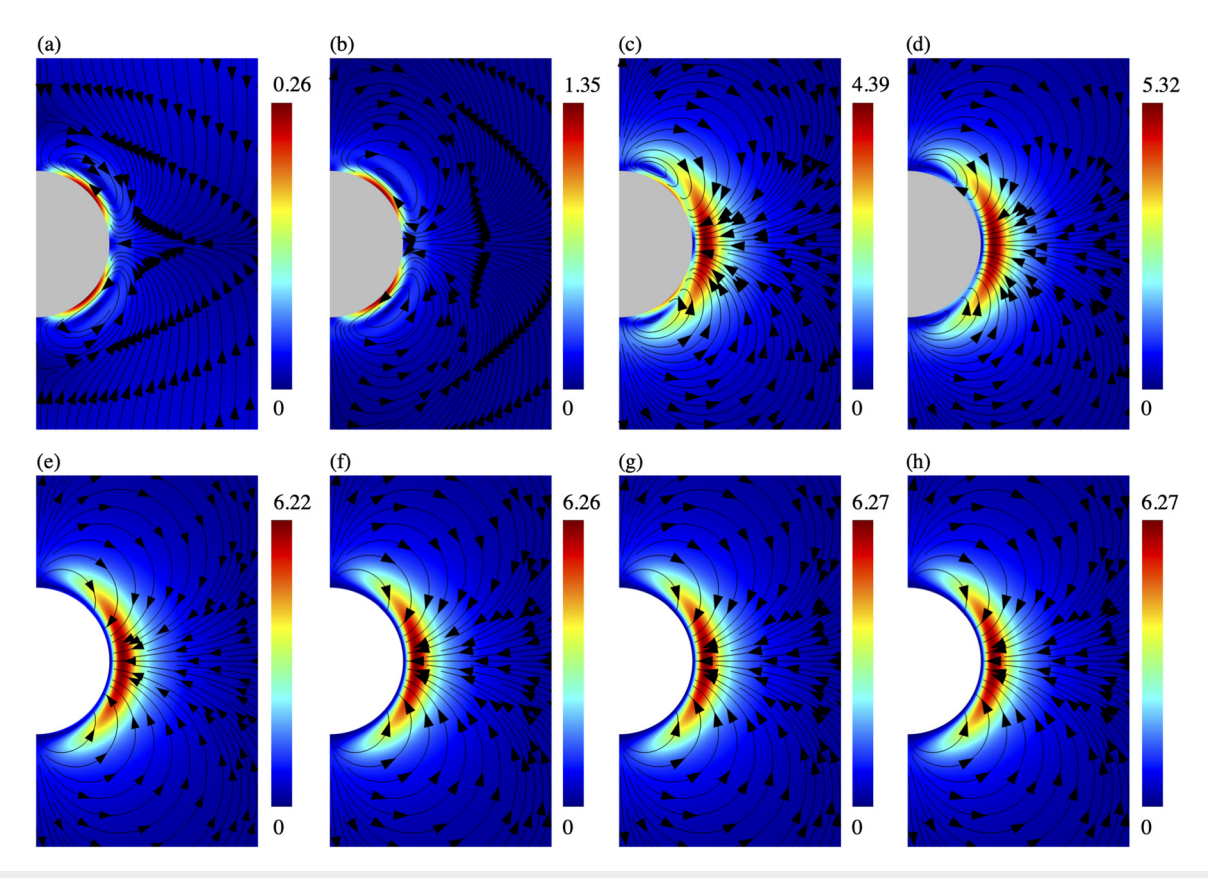


FIG. 7. Impact of oscillation dynamics on time-averaged radiation force field for four different material choices: [(a) and (e)] PDMS, [(b) and (f)] PMMA, [(c) and (g)] copper, and [(d) and (h)] gold. The results are obtained with oscillation dynamics predicted from (a)–(d) the fluid–solid model and (e)–(h) the impedance model. The color legends indicate the magnitude in pN.

factor of the scatterer material increases, the center of the vortices moves closer to the interface. These vortices vanish completely in the limit of a rigid scatterer, as shown in our prior report. In contrast, the vortices are absent in the impedance solution irrespective of the material choice. These results agree well with our results in Secs. III A and III B where the impedance model failed to fully capture the compliant nature of the interface and predicted results that are representative of a rigid scatterer material.

Next, we turn our attention on the streaming velocity predicted from the two models as shown in Fig. 8. Referring to Figs. 8(a)-8(d), the solution from the fluid-solid model is characterized by two pair of vortices in the vicinity of the scatterer, and the innermost pair of vortices become progressively smaller with increase in the acoustic contrast factor. In contrast, the impedance solution exhibits only one pair of vortices for all material choices. Again, while the fluid-solid model results vary significantly among different material choices, the impedance model results are qualitatively indifferent to material choice and are similar to those obtained in the limit of rigid material.

Overall, these results illustrate the inability of the impedance model in accurately capturing the fluid–solid interfacial dynamics. The impedance model may represent a good approximation to the fluid– solid solution in the limit of rigid materials where the material can be considered to be locally reactive to the acoustic waves. Nonetheless, its predictions diverge both qualitatively and quantitatively from the fluid-solid solution for scatterer materials with low acoustic contrast factor. This is a significant finding since the impedance model has been commonly used to approximate materials with relatively low acoustic contrast factor such as PDMS in the context of surface acoustic wave devices. ^{12,13,15} Furthermore, our analysis also reveals that even the materials that are typically viewed as being rigid in acoustofluidics literature (e.g., glass) are not sufficiently close to the rigid limit for the impedance condition to be a good approximation of the fluid-solid interface.

IV. CONCLUSION

We presented a numerical study to investigate the efficacy of impedance boundary conditions for modeling oscillatory dynamics and time-averaged fields around a particle subjected to a standing acoustic wave. To this end, we compared the numerical results obtained via an impedance boundary approach against those obtained by a coupled fluid-solid approach. We systematically elucidated the inherent assumptions in the derivation of the impedance boundary condition and contrasted the treatment of fluid-solid interface in the two models. The acoustic response obtained from both models is subsequently utilized to obtain the system's corresponding time-averaged response.

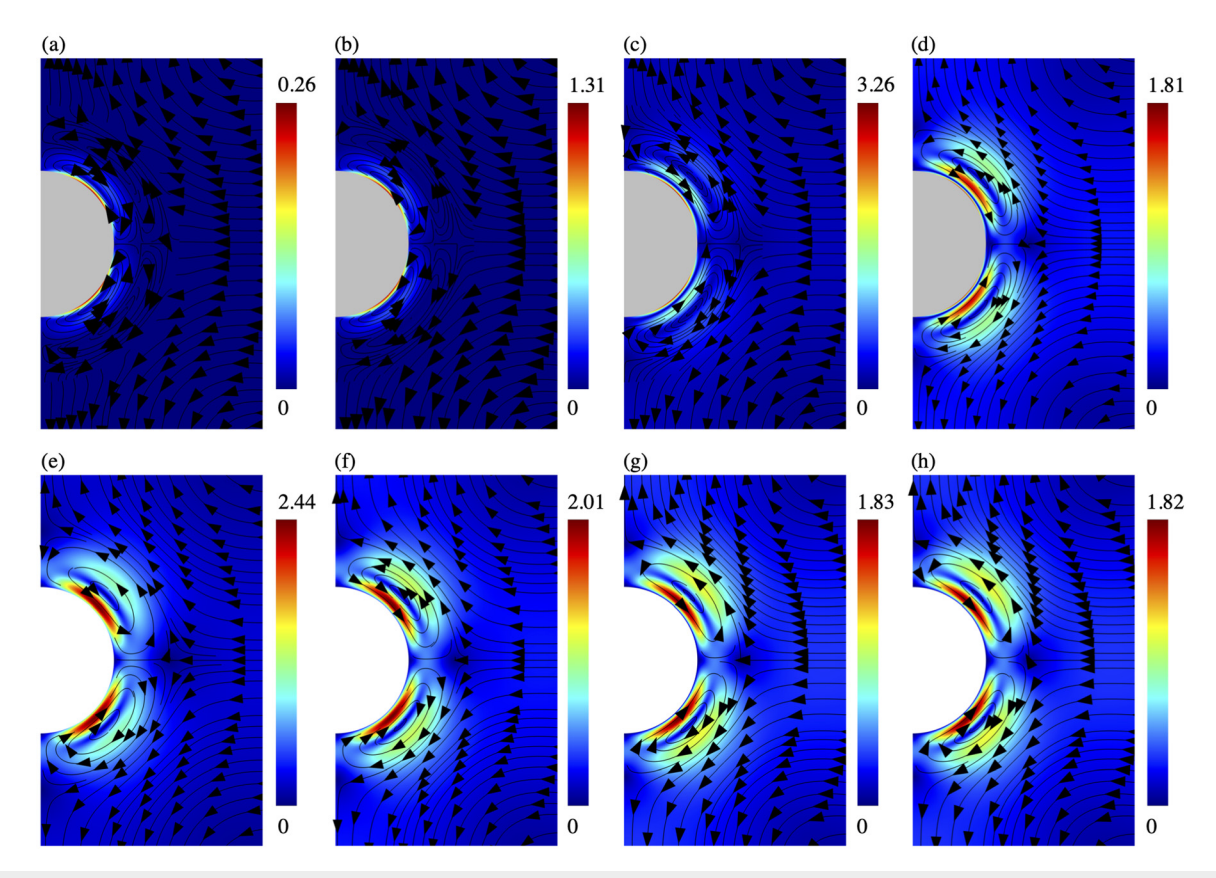


FIG. 8. Impact of oscillation dynamics on streaming field for four different material choices: [(a) and (e)] PDMS, [(b) and (f)] PMMA, [(c) and (g)] copper, and [(d) and (h)] gold. The results are obtained with oscillation dynamics predicted from (a)–(d) the fluid–solid model and (e)–(h) the impedance model. The color legends indicate the magnitude in mm/s.

We first considered a representative system comprising of a glass scatterer immersed in water to demonstrate that while impedance model may predict qualitatively similar results to the coupled fluid-solid model for the oscillatory acoustic fields, the results differ significantly from a quantitative perspective. A closer inspection of the results from the two models reveals significant differences in the oscillatory fluid-solid interfacial dynamics. These differences further lead to time-averaged fields that differ both qualitatively and quantitatively between the two models.

We also investigated the discrepancies in the time-averaged fields by varying the scatterer materials. To this end, we considered four different materials with increasing acoustic contrast factor with respect to the surrounding fluid. Our results revealed that the impedance model fails to completely capture the interface compliance. Interestingly, the impedance boundary approach yielded results that are relatively insensitive to the scatterer material and are qualitatively similar to the rigid limit. This is a noteworthy result since the impedance model is typically employed to approximate materials with relatively low acoustic contrast factors (e.g., PDMS), where its predictions diverge significantly from the fluid–solid model.

Finally, given the results in Figs. 2-6, we remark that qualitative similarity between numerical modeling choices should not be used to justify the general applicability of impedance boundary conditions. Specifically, given the qualitative similarity observed in Fig. 2, it might be tempting to simply scale the results of impedance model to match the predictions of the fully coupled model or the experimental data (when available). Similar scaling has also been proposed for numerical models by Ni et al.²⁴ in the context of surface acoustic wave devices. However, the results presented here illustrate that despite being acceptable for the specific device considered by Ni et al.,24 such scaling must be employed with caution as it might not be generally applicable for different fluid-solid material combinations. Overall, our results emphasize the need to exercise caution in the use of impedance boundary conditions and suggest conducting quantitative comparisons against experimental data or fully coupled numerical models to ascertain their validity.

In future, this study can be extended to include several specific physical considerations that have not been examined here. For instance, a straightforward extension would be to translate the findings of this study for a particle subjected to traveling acoustic waves. Furthermore, different particle shapes and sizes can be considered to investigate the impact of scatterer size and viscous boundary layer effects. The findings reported in this work are also expected to lead to further investigations in the context of specific acoustofluidic devices by incorporating the presence of channel walls, multiparticle interactions, wall enhancement effects of viscous drag, viscous–acoustic interactions, and thermoviscous effects.

SUPPLEMENTARY MATERIAL

See the supplementary material for results concerning the benchmarking of our numerical model against the available analytical and experimental data.

ACKNOWLEDGMENTS

This work was supported by the National Science Foundation (No. OIA-2229636), the Jane Robertson Layman Fund at the

University of Nebraska Foundation, and the Nebraska Center for Integrated Biomolecular Communication (NIH National Institutes of General Medical Sciences No. P20 GM113126).

AUTHOR DECLARATIONS

Conflict of Interest

The authors have no conflicts to disclose.

ARTICLE

Author Contributions

Khemraj Gautam Kshetri: Conceptualization (equal); Investigation (equal); Methodology (equal); Software (equal); Visualization (lead); Writing – original draft (equal); Writing – review & editing (equal). Nitesh Nama: Conceptualization (equal); Funding acquisition (lead); Investigation (equal); Methodology (equal); Project administration (lead); Software (equal); Supervision (lead); Writing – original draft (equal); Writing – review & editing (equal).

DATA AVAILABILITY

The data that support the findings of this study are available within the article and its supplementary material.

REFERENCES

- ¹X. Ding, P. Li, S.-C. S. Lin, Z. S. Stratton, N. Nama, F. Guo, D. Slotcavage, X. Mao, J. Shi, F. Costanzo *et al.*, "Surface acoustic wave microfluidics," Lab Chip 13, 3626–3649 (2013).
- ²T. Laurell and A. Lenshof, *Microscale Acoustofluidics* (Royal Society of Chemistry, 2014).
- ³N. Nama, P.-H. Huang, T. J. Huang, and F. Costanzo, "Investigation of acoustic streaming patterns around oscillating sharp edges," Lab Chip 14, 2824–2836 (2014).
- ⁴P.-H. Huang, Y. Xie, D. Ahmed, J. Rufo, N. Nama, Y. Chen, C. Y. Chan, and T. J. Huang, "An acoustofluidic micromixer based on oscillating sidewall sharpedges," Lab Chip 13, 3847–3852 (2013).
 ⁵I. Leibacher, P. Hahn, and J. Dual, "Acoustophoretic cell and particle trapping
- 5I. Leibacher, P. Hahn, and J. Dual, "Acoustophoretic cell and particle trapping on microfluidic sharp edges," Microfluid. Nanofluid. 19, 923–933 (2015).
- ⁶D. Ahmed, A. Ozcelik, N. Bojanala, N. Nama, A. Upadhyay, Y. Chen, W. Hanna-Rose, and T. J. Huang, "Rotational manipulation of single cells and organisms using acoustic waves," Nat. Commun. 7, 11085 (2016).
- ⁷C. Dillinger, N. Nama, and D. Ahmed, "Ultrasound-activated ciliary bands for microrobotic systems inspired by starfish," Nat. Commun. 12, 6455 (2021).
- ⁸J. Durrer, P. Agrawal, A. Ozgul, S. C. Neuhauss, N. Nama, and D. Ahmed, "A robot-assisted acoustofluidic end effector," Nat. Commun. 13, 6370 (2022).
- ⁹H. Bruus, "Acoustofluidics 7: The acoustic radiation force on small particles," Lab Chip 12, 1014–1021 (2012).
- ¹⁰P. B. Muller, R. Barnkob, M. J. H. Jensen, and H. Bruus, "A numerical study of microparticle acoustophoresis driven by acoustic radiation forces and streaming-induced drag forces," Lab Chip 12, 4617–4627 (2012).
- ¹¹B. Hammarström, M. Evander, H. Barbeau, M. Bruzelius, J. Larsson, T. Laurell, and J. Nilsson, "Non-contact acoustic cell trapping in disposable glass capillaries," Lab Chip 10, 2251–2257 (2010).
- ¹²N. Nama, R. Barnkob, Z. Mao, C. J. Kähler, F. Costanzo, and T. J. Huang, "Numerical study of acoustophoretic motion of particles in a PDMS microchannel driven by surface acoustic waves," <u>Lab Chip</u> 15, 2700–2709 (2015).
- ¹³C. Chen, S. P. Zhang, Z. Mao, N. Nama, Y. Gu, P.-H. Huang, Y. Jing, X. Guo, F. Costanzo, and T. J. Huang, "Three-dimensional numerical simulation and experimental investigation of boundary-driven streaming in surface acoustic wave microfluidics," Lab Chip 18, 3645–3654 (2018).
- ¹⁴N. R. Skov and H. Bruus, "Modeling of microdevices for saw-based acoustophoresis—A study of boundary conditions," Micromachines 7, 182 (2016).
- 15 C. Devendran, T. Albrecht, J. Brenker, T. Alan, and A. Neild, "The importance of travelling wave components in standing surface acoustic wave (SSAW) systems," Lab Chip 16, 3756–3766 (2016).

- ¹⁶F. Guo, Z. Mao, Y. Chen, Z. Xie, J. P. Lata, P. Li, L. Ren, J. Liu, J. Yang, M. Dao et al., "Three-dimensional manipulation of single cells using surface acoustic waves," Proc. Natl. Acad. Sci. U. S. A. 113, 1522–1527 (2016).
- ¹⁷S. Sachs, M. Baloochi, C. Cierpka, and J. König, "On the acoustically induced fluid flow in particle separation systems employing standing surface acoustic waves-Part I," Lab Chip 22, 2011–2027 (2022).
- ¹⁸R. Barnkob, N. Nama, L. Ren, T. J. Huang, F. Costanzo, and C. J. Kähler, "Acoustically driven fluid and particle motion in confined and leaky systems," Phys. Rev. Appl. 9, 014027 (2018).
- ¹⁹M. R. Dezfuli and A. Shahidian, "Numerical investigation of acoustic streaming vortex and operating parameters in curved microchannel: Driven by standing surface acoustic wave," Eur. Phys. J. Plus 138, 835 (2023).
- 20Z. Mao, Y. Xie, F. Guo, L. Ren, P.-H. Huang, Y. Chen, J. Rufo, F. Costanzo, and T. J. Huang, "Experimental and numerical studies on standing surface acoustic wave microfluidics," Lab Chip 16, 515–524 (2016).
- ²¹B. E. Treeby, J. Pan, and R. M. Paurobally, "Acoustic scattering by a sphere with a hemispherically split boundary condition," J. Acoust. Soc. Am. 122, 46–57 (2007).
- ²²J. Wang, X. Zhang, and G. Zhang, "Acoustic radiation force of a sphere with a hemispherically split boundary condition in a plane wave," J. Acoust. Soc. Am. 152, 501–510 (2022).
- 23 [Liebacher, S. Schatzer, and J. Dual, "Impedance matched channel walls in acoustofluidic systems," Lab Chip 14, 463–470 (2014).
- ²⁴Z. Ni, C. Yin, G. Xu, L. Xie, J. Huang, S. Liu, J. Tu, X. Guo, and D. Zhang, "Modelling of SAW-PDMS acoustofluidics: Physical fields and particle motions

- influenced by different descriptions of the PDMS domain," Lab Chip 19, 2728–2740 (2019).
- 25Y. Zhou, "Comparison of numerical models for bulk and surface acoustic waveinduced acoustophoresis in a microchannel," Eur. Phys. J. Plus 135, 696 (2020).
- ²⁶W. L. Nyborg, "Acoustic streaming near a boundary," J. Acoust. Soc. Am. 30, 329–339 (1958).
- ²⁷T. Baasch, A. Pavlic, and J. Dual, "Acoustic radiation force acting on a heavy particle in a standing wave can be dominated by the acoustic microstreaming," Phys. Rev. E 100, 061102 (2019).
- ²⁸K. G. Kshetri and N. Nama, "Acoustophoresis around an elastic scatterer in a standing wave field," Phys. Rev. E 108, 045102 (2023).
- ²⁹M. Settnes and H. Bruus, "Forces acting on a small particle in an acoustical field in a viscous fluid," Phys. Rev. E 85, 016327 (2012).
- ³⁰A. Pavlic, P. Nagpure, L. Ermanni, and J. Dual, "Influence of particle shape and material on the acoustic radiation force and microstreaming in a standing wave," Phys. Rev. E 106, 015105 (2022).
- ⁵¹N. Nama, T. J. Huang, and F. Costanzo, "Acoustic streaming: An arbitrary lagrangian-eulerian perspective," J. Fluid Mech. 825, 600–630 (2017).
- ³²H. Bruus, "Acoustofluidics 2: Perturbation theory and ultrasound resonance modes," Lab Chip 12, 20–28 (2012).
- ³³A. R. Selfridge, "Approximate material properties in isotropic materials," IEEE Trans. Sonics Ultrason. 32, 381–394 (1985).
- ³⁴A. Pavlic, L. Ermanni, and J. Dual, "Interparticle attraction along the direction of the pressure gradient in an acoustic standing wave," Phys. Rev. E 105, L053101 (2022).